Journal Name

ARTICLE TYPE

Cite this: DOI: 00.0000/xxxxxxxxxx

Ensemble Effects on Allylic Oxidation Within Explicit Solvation Environments

Hung M. Le,* *a Mariano Guagliardo, b‡ Anne E. V. Gorden, b‡ and Aurora E. Clark* *a,c

Received Date **Accepted Date**

DOI: 00.0000/xxxxxxxxxx

Umbrella-sampling density functional theory molecular dynamics (DFT-MD) has been employed to study the full catalytic cycle of the allylic oxidation of cyclohexene using a Cu(II) 7-amino-6-((2hydroxybenzylidene)amino)quinoxalin-2-ol complex in acetonitrile to create cyclohexenone and H₂O as products. After the initial H-atom abstraction step, two different reaction pathways have been identified that are distinguished by the participation of alkyl hydroperoxide (referred to as the "open" cycle) versus the methanol side-product (referred to as the "closed" cycle) within the catalyst recovery process. Importantly, both pathways involve dehydrogenation and re-hydrogenation of the -NH2 group bound to the Cu-site - a feature that is revealed from the ensemble sampling of configurations of the reactive species that are stabilized within the explicit solvent environment of the simulation. Estimation of the energy span from the experimental turnover frequency yields an approximate value of 22.7 kcal/mol at 350 K. Whereas the closed cycle value is predicted to be 26.2 kcal/mol, the open cycle value at 16.5 kcal/mol. Both pathways are further consistent with the equilibrium between Cu(II) and Cu(III) than what has previously been observed. In comparison to prior static DFT calculations, the ensemble of of both solute and solvent configurations has helped to reveal a breadth of processes that underpin the full catalytic cycle yielding a more comprehensive understanding of the importance of radical reactions and catalysis recovery.

Introduction 1

The oxidation of an allylic -CH2 group to a carbonyl is an important process in multi-step organic syntheses, 112 consider that α,β -unsaturated enones or 1,4-enediones have been utilized as essential building components in the synthesis of numerous natural compounds and drug precursors. 3-7 In general, allylic oxidation can be efficiently activated using tert-butyl hydroperoxide (TBHP) with the addition of metal catalysts. 8-13 Cu(II) complexes have been of particular interest as copper is relatively economical and environmentally benign. For example, Yao et al. 14 synthesized a stable aryl-Cu(III) complex that was employed for C-H activation, resulting in very good yields under aerobic conditions. Wang and coworkers have synthesized a Cu(II) complex for dehydrogenative aminooxygenations, wherein the Cu oxidation state was demonstrated to convert from (Cu(II) to Cu(III)). 15 By allowing a Cu(II)-superoxide complex to react with acyl chlo-

The catalyst of interest in this work is Cu(II) 7-amino-6-((2-hydroxybenzylidene)amino)quinoxalin-2-ol, first reported in 2014. This catalyst was developed to limit interference from free radical reactions; at the same time, it was found to demonstrate excellent efficiency in allylic oxidation reactions. However,

ride substrates, Pirovano and co-workers found the resultant complex to be a reactive nucleophile, which could be subsequently be employed for Baeyer–Villiger oxidations of aldehydes. 16 More recently, C-H bond activation of methylene groups has been achieved using a triazole based ligand and mCPBA, 17 and a bioinspired Cu(II) complex has been used in the hydroxylation of benzene under mild conditions. [18] With the aim of developing new, economically advantageous catalysts possessing increased sustainability for allylic oxidations, Wu and co-workers [19] developed a Cu(II) 2-quinoxalinol salen complex which completed the oxidation of allylic species without the common additional requirements of high heat or long reaction times. In a subsequent study, such a catalyst was applied with TBHP as an oxidant, and the oxidation of a variety of olefin substrates was reported with high yields. 20 The use of Cu(II) catalysts in the functionalization of organic structures both with and without the addition of peroxides has also recently been reviewed. 21 A detailed analysis of such catalytic mechanisms can provide an improved understanding of their nature, and subsequently lead to the strategic design of new improved catalysts.

^a Department of Chemistry, Washington State University, Pullman, Washington 99164, United States

^b Department of Chemistry and Biochemistry, Texas Tech University, Lubbock, Texas 79430. United States

^c Pacific Northwest National Laboratory, Richland, Washington 99352, United States Email: hung.le2@wsu.edu, auclark@wsu.edu

[†] Electronic Supplementary Information (ESI) available: See DOI: 00.0000/00000000.

static density functional theory (DFT) calculations of the reaction mechanism in a continuum description of acetonitrile resulted in a relatively high estimation of reaction barriers; the H-abstraction step was reported to consume 43.7 kcal/mol, while the step to release cyclohexenone required 37.5 kcal/mol. Further, the final steps to retrieve the initial catalytic structure was not described. Estimating the turnover number (TON) from the amount of catalyst used and the yield, results in an approximate turnover frequency (TOF) of 190/hour that, when employed with the Eyring equation, yields an approximate energy span^[23] of 22.7 kcal/mol.

In recent years, DFT-based molecular dynamics 24125 (DFT-MD) have achieved sufficient computational efficiency to support broader application in the study of catalytic cycles that account for the ensemble and dynamic evolution of solvent and solutes. This method is a significant improvement over more widespread embedding methods that attempt to include solvent effects by placing the solute of interest within a dielectric continuum. In the latter, direct solute-solvent interactions are not considered, which hampers the study of catalytic processes where the solvent may play a more prominent role. Further, the ensemble sampling of solute and solvent configurations can reveal important mechanistic features that are not observed when taking a more prescribed approach that involves a pre-defined reaction coordinate with limited degrees of freedom.

The current work employs DFT-MD to elucidate two new reaction schemes for the allylic oxidation of cyclohexene that have significantly lowered free energies for reaction relative to the prior static DFT studies, and they further sample multiple reaction pathways. The cycles are differentiated by the participation of alkyl hydroperoxide (leading to the "open" cycle) versus the methanol side-product (leading to the "closed" cycle) within the catalyst recovery process. In both cases, supporting evidence is provided for the previously reported electronic structure changes reported by Storr et al. 27 of square planar Cu(II) that undergoes reversible oxidation to Cu(III) during the course of the C-H bond activation. The recovery of methyl peroxide (CH3OO-) attached to the Cu site is obtained to complete the catalytic cycle. The new reaction schemes involve the bound -NH2 of the ligand acting as an H-atom reservoir. The energy span of the closed cycle value is predicted to be 26.2 kcal/mol while the open cycle lies at 16.5 kcal/mol.

2 Computational Details

2.1 MD Simulation Protocol

The Cu(II) 7-amino-6-((2-hydroxybenzylidene)amino)quinoxalin-2-ol complex (1) is a slightly simplified catalyst model with respect to the experimental system, wherein the two t-butyl groups (-C(CH₃)₃) on the quinoxalin-2-ol and salicylidene residues are replaced by -H because they are far from the reactive site that consists of Cu(II) and the attached methyl hydroperoxide (-OOCH₃). The optimized molecular structure of catalyst 1 is shown in Figure 1 along with the subsequent reaction intermediates (*vide infra*).

The catalyst, reactants, and 60 acetonitrile (357 atoms in total) are initialized by random insertion into a periodic cubic

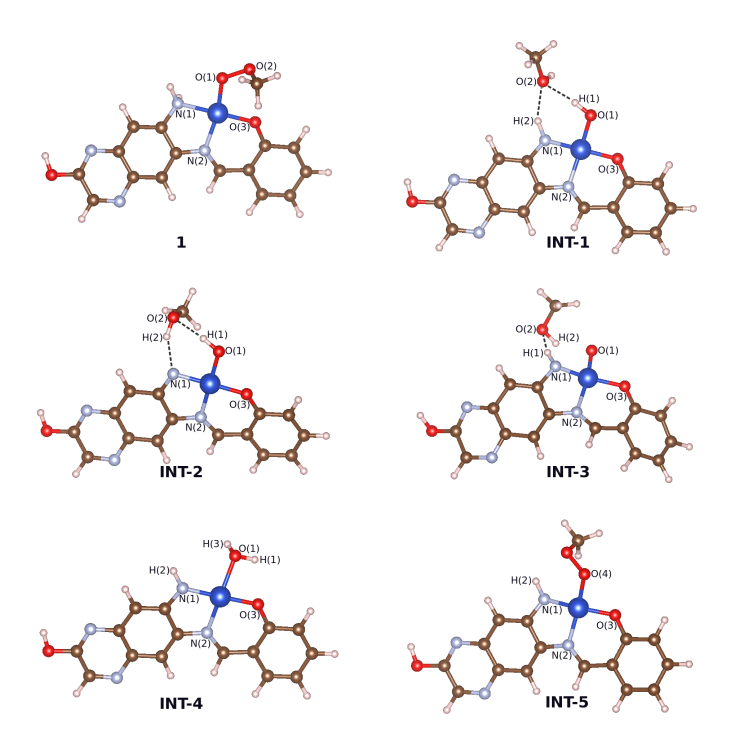


Fig. 1 Molecular structure of catalyst 1 (1) Cu(II) 7-amino-6-((2-hydroxybenzylidene)amino)quinoxalin-2-ol, and the five subsequent intermediates INT-1, INT-2, INT-3, INT-4, INT-5. Color codes for atomic representation: Cu (deep blue), C (brown), O (red), N (light blue), hydrogen (white). The $O(4)OCH_3$ residue is originated from the reaction with a new methyl hydroperoxide molecule.

box using the Packmol code. 28 The size of the periodic box with edge-length of 17.5 Å is obtained as a result of system equilibration using the NPT-ensemble with the stochastic velocity rescaling method within DFT-MD for 2 ps at 350 K (the experimental temperature²²), in the Quantum Espresso package. 30 The PBE functional 31-33 was employed with the DFT-D3, long-range London dispersion interaction classical interaction scheme proposed by Grimme, 34 to provide empirical correction terms to the long-range interactions. The use of this well-established generalized-gradient-approximation functional with the D3 correction guarantees reasonable chemical intuition as well as computational expense for umbrella sampling MD. The Rappe-Rabe-Kaxiras-Joannopoulos ultrasoft (RRKJUS) plane-wave basis set and pseudo-potential was employed for all participant atoms. To compromise with computational expense for such a large system, we use Γ -point calculations. A standard time step of 20 atomic Rydberg time-units (~ 0.968 fs) is used at every MD step, and the Verlet integration method 38 is employed to integrate the classical equations of motion. The density of the NPT equilibrated system is 0.77 g/cm³. The slightly low density relative to experimental bulk acetonitrile (density = 0.79 g/cm³) is anticipated based upon the small simulation box size wherein about 20% of the volume is occupied by the solute molecules.

2.2 Umbrella Sampling of the Catalytic Cycle

The umbrella sampling technique 39-41 enhances sampling along a specific reaction channel and employs the NVT ensemble at the experimental temperature of 350 K, 22 using the velocity rescaling thermostat. 42 In each bin, we apply a harmonic-bias potential to put a constraint on the chosen reaction coordinate. The reaction coordinate varies for each step in the catalytic cycle and is described in the Results and Discussion. Each harmonic potential adopts the form:

$$V(\chi) = \frac{1}{2}\kappa(\chi - \chi_e)^2,\tag{1}$$

where κ is the spring constant (kcal/Å²), and χ_e is the location for constraining the reaction coordinate (Å). To obtain good statistical data in umbrella sampling, the bin size is 0.1 Å, and 200 DFT-MD steps are sampled in each bin. To verify that the use of 200 DFT-MD steps is sufficient for the convergence of free energy approximation, we carry out several tests with various number of DFT-MD steps (150-200) for each reaction step as shown by Figures S1 S6 in the Supporting Information. The overlap of umbrella-sampling bins are presented in Figures S7 S12

From the biased MD data obtained at each step, the average distribution function can be computed statistically through a Boltzmann-weighted scheme:

$$\langle \rho(\chi_e) \rangle = \frac{\int \delta(\chi_e - \chi) e^{-V(q)/k_B T} dq}{\int e^{-V(q)/k_B T} dq},$$
 (2)

In the above equation, k_B is the Boltzmann constant, and T is the chosen temperature (350 K) for simulation. Then, the potential of mean force (PMF) demonstrating the free-energy profile for a reaction along the user-defined internal coordinate χ can be calculated: 43

$$\omega(\chi) = -k_B T \ln(\langle \rho(\chi) \rangle), \tag{3}$$

For the investigated reaction channels in this study, the PMF approximations which follow equations 2 and 3 are executed using the weighted-histogram analysis method (WHAM) as implemented by Grossfield. 44 45

The energetic span of a catalytic cycle was conceptualized by Kozuch and Shaik²³, and places an emphasis upon the energetic profile associated with the turn-over-frequency (TOF). To determine an energetic span, the TOF-determining structure (TDS) and TOF-determining transition state (TDTS) must be determined. Within the reactions studied in this work, the TDTS appears after TDS, thus, the energetic span of the reaction cycle is defined as: 23

$$\delta E = G_{\rm TDTS} - G_{\rm TDS},\tag{4}$$

where G_{TDTS} and G_{TDS} represent the free energy of TDTS and TDS, respectively.

2.3 Static DFT calculations

Static DFT calculations were performed to validate the prior work of Li et al. 22 and explore differences in energy barriers for Hatom abstraction from cyclohexene. Gas-phase geometry optimizations using either B3LYP/6-31G(d), B3LYP-D3/6-31G(d) and PBE-D3/6-31G(d) were performed for cyclohexene, the catalyst 1, and the H-atom abstraction transition state based upon abstraction by the bound peroxo O(1) atom (see Figure 1). For each of the calculation set above, two different single-point calculations using the the $6-311+G(2df,p)^{46/47}$ basis set were then performed in the gas phase and using the Solvation Model based on Density approximation (SMD) the polarizable continuum model (PCM). 49 The same set of calculations were also compared using four acetonitrile molecules surrounding the reactant, transition state, and product, so as to evaluate the impact of explicit solvation when combined with a PCM.

Results and Discussion

As previously advocated by Kozuch and Shaik²³, we consider the entire energy span of the catalytic cycle - including potential branch points - so as to elucidate the most favorable reaction cycle (including catalyst recovery) and understand the consistency of different mechanisms with the available experimental TOF data.

3.1 Formation of cyclohexenone

The H-atom abstraction of cyclohexene was first investigated via attack by the peroxo- ligand attached to Cu(II), to form the cyclohexene radical. Within the umbrella sampling, two different abstraction steps are considered, where the reaction coordinate consists of either the allylic H-site being approached by O(1) or O(2) of the catalyst (atom labels denoted in Figure 1) and establishing a new O-H bond, thus breaking the O-O bond. The cyclohexene hydrogen is initially placed 4.8 Å from O(1) or O(2), and using a window size of 0.1 Å the distance is systematically decreased. In the initial stage having $r_{O(1)-H}$ or $r_{O(2)-H}$ (≥ 2.7 Å), a force constant for the harmonic bias of ($\kappa = 50 \text{ kcal/mol}\text{Å}^2$) is employed, which is increased to 100 kcal/molÅ², and at the transition state of new O-H bond formation (around 1.2 Å), a high force constant of 400 kcal/molÅ² is used. It is practical to perform manual tuning of the harmonic constant during umbrella sampling to enforce good overlap between distance bins. 50 The long-range interactions at large distances are weak and require only a small κ , whereas the formation of a hydroxide (O-H) covalent bond at short distances necessitates a large κ . As shown in Figure 2(a), the PMF curve of the O(1)...H channel of 1 shows a free energy barrier of 12.1 \pm 0.2 kcal/mol, which is more favorable than the O(2)...H channel at 15.6 \pm 0.4 kcal/mol.

Alternatively, this step can be examined using the ideal gasrigid rotor-harmonic oscillator (IGRRHO) method, in which entropy is established using the rigid rotor or harmonic oscialltor approximation. As shown in a previous study of the ligand exchange process in the palladium complexes, 51 the IGRRHO method gave reasonable estimation of free energy in comparison with that given by umbrella sampling DFT-MD for the same exchange reaction. In the H abstraction case, the O(1)-H reaction step was previously investigated using the IGRRHO method with gas-phase optimized B3LYP and single-point SMD polarizable continuum (PCM) approximations to the acetonitrile media, where a free energy barrier of 43.7 kcal/mol was predicted. [22] To investigate the significant variation in the predicted barriers, we first employed the same computational protocol and nominally

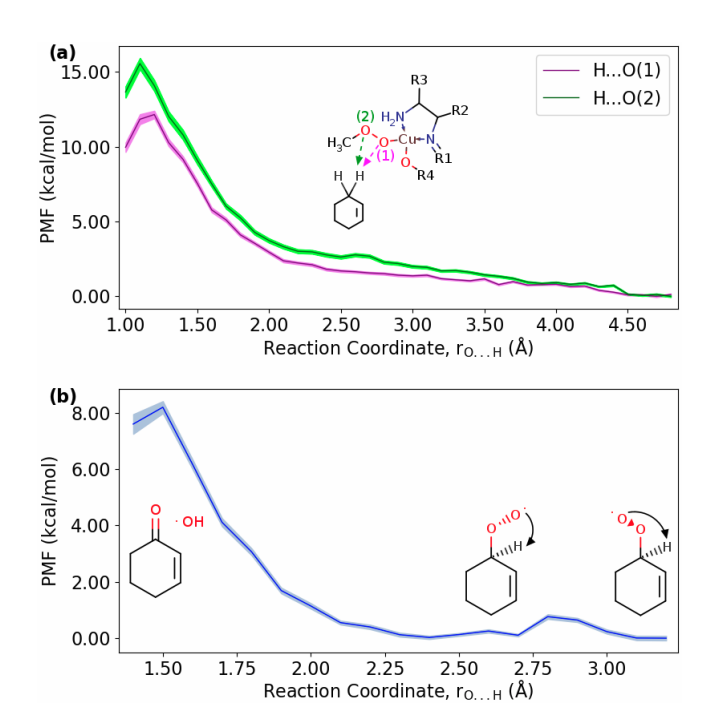


Fig. 2 (a) PMF for O(1)...H and O(2)...H abstraction channels by catalyst 1, (b) PMF for the formation of cyclohexenone and $\cdot OH$ radical.

reproduced their barrier height, with a predicted ΔG^{\dagger} (SMD, 298) K) of 45.8 kcal/mol. Examination of the solvation energy correction revealed an \approx 8 kcal/mol variation for the reactants (determined in separate single-point calculations with their own individual solute cavities embedded within the solvent continuum) versus the transition state (having a single cavity), which serves to increase the activation barrier ≈ 7 kcal/mol (for both ΔE^{\dagger} and ΔG^{\dagger}). To learn the impact of dispersion interactions on the energetics of this catalytic step, we performed the same set of calculations using B3LYP-D3, and observed a consistent drop of > 10 kcal/mol in both ΔE^{\dagger} and ΔG^{\dagger} in comparison with the B3LYP results in Table 1. In addition, we also performed the static PBE-D3 calculations, which reduced the activation barrier by a remarkable \approx 20 kcal/mol in comparison with the B3LYP result, with the same observations regarding the solvation correction. We then included 4 explicit CH₃CN within the gas-phase geometry optimization of the reactants and transition state using the PBE-D3 functional, followed by SMD solvation corrections. Notably, the explicit solvent calculation led to a decrease in ΔE^{\dagger} , even after the PCM correction. This is the opposite effect that the PCM had upon the ΔE^{\dagger} in the absence explicit solvent. These data indicate that the significant variation in the cavity size for the reactants and transition state leads to incomplete error cancellation within the PCM approach that supports an artificially increased predicted barrier from the static DFT calculations. The entropic contribution to the free energy is also significant in these calculations (T Δ S \approx 10 kcal/mol in the implicit PCM calculations and ≈15 kcal/mol in the case with 4 CH₃CN). Indeed, similar magnitude of T\DeltaS contribution were observed for numerous elementary dissociations/associations. 52 Note that in the static calculations the entropic contributions are approximated from ideal gas and

Scheme 1 Two reaction channels of 1 associated with the O(1) or O(2) abstraction of the allylic cyclohexene hydrogen lead to the formation of cyclohexene radical and methanol, and INT-1.

harmonic partition functions, while the ensemble distribution of states is explicitly determined in the DFT-MD. Thus, we also posit that the entropic contributions in the static DFT calculations also contribute significantly to the much higher calculated ΔG^{\dagger} relative to the DFT-MD simulations. In combination, the nearly 30 kcal/mol decrease in ΔG^{\dagger} from the PMF simulations relative to the previously reported static DFT calculations is attributed to three sources: 1) changes in the density functional, 2) incomplete error cancellation in the PCM, and 3) variations in the way in which the entropic contributions are considered.

Notably, the TS for H-atom abstraction is nominally the same in the prior static calculations as in this work; however, after the TS, the gas-phase reactivity of the CH₃O· leads to it binding to the Cu(II) site with dissociation of the bound -NH2 of the ligand to maintain a 4-coordinate Cu-center. In contrast, following the first reaction channel of O(1) abstraction with DFT-MD, a hydroxyl (-OH) residue is established at the O(1) site, which bonds directly to Cu(II), while CH₃O(2)· quickly abstracts the hydrogen atom from the bound $N(1)H_2$ of the ligand to produce methanol. This is a fast and spontaneous process that occurs within 0.2 ps after the O(1)-O(2) dissociation. In the second reaction channel, based upon the O(2) allylic H-atom abstraction, an alcohol residue is established at O(2). Methanol would be produced directly as a product of this reaction step, while the resulting O(1) radical quickly abstracts a hydrogen atom from the nearby -N(1)H2 to become -O(1)-H bound to the Cu. Thus, somewhat surprisingly, both of the reaction channels from O(1) and O(2) abstractions lead to the formation of methanol and Cu-O-H, and the dehydrogenation of the coordinated $-N(1)H_2$ to -N(1)H (see Scheme 1). The intermediate Cu-complex is labeled as INT-1 obtained from catalyst 1, as illustrated in Figure 1. The unique dehydrogenation behavior is revealed by the ensemble sampling of different degrees of freedom of the solutes and solvent, which would not be anticipated from a static DFT study. Also, note that the CH₃O(2)H molecule that has been formed from the dehydrogenation of -N(1)H₂ remains hydrogen bonded to the INT-1 structure (as is shown in the radial distribution function (RDF) plots in Figure \$14). This important feature has the ability to support H-atom transfer in later reaction steps.

The cyclohexene radical that is produced by H-atom abstraction is most likely oxidized by either molecular oxygen or an external CH_3OOH to form cyclohexenone. Prior experimental study employed ^{18}O labelled O_2 and found a ratio of labelled to unla-

Table 1 Total electronic energies (kcal/mol) and free energy (kcal/mol) at 298 K and 350 K for the O(1)-H abstraction.

H-atom abstraction (TS - reactants)	E(298/350)	E(PCM, 298/350)	G(298/350)	G(PCM, 298/350)
B3LYP (no explicit solvent)	27.6 / 27.6	34.4 / 34.4	39.0 / 40.9	45.8 / 47.7
B3LYP-D3 (no explicit solvent)	15.4 / 15.4	22.6 / 22.6	29.4 / 31.9	36.7 / 39.2
PBE-D3 (no explicit solvent)	9.6 / 9.6	16.4 / 16.4	20.7 / 22.6	27.6 / 29.4
PBE-D3 (4 explicit solvent molecules)	3.5 / 3.5	13.0 / 13.0	21.5 / 24.8	31.0 / 34.3
	DFT-MD (350)	12.1		

belled ¹⁸O-cyclohexenone of 1:3. Although this supports a preference for oxidation by CH3OOH, the resulting radical chemistry is significantly more complicated, and hence, we focused on the reaction channel with molecular O2 to investigate cyclohexenone formation and subsequent catalyst recovery. The system containing INT-1, molecular oxygen and the cyclohexene radical was equilibrated for 1.5 ps at 350 K, wherein the O2 diffused to the cyclohexene radical and reacted to form the cyclohexene-peroxo radical. This species adopts a trans conformation about the O-O-C-H and as such, the equilibrium distance between the terminal oxygen atom and allylic hydrogen atom is 3.2 Å. A rotational barrier must exist along this dihedral, as rotation does not readily occur. Thus, this species is somewhat long-lived and prevents the observation of further reaction within the 1.5 ps of equilibrated trajectory. Umbrella sampling was then performed that brought the terminal O-atom to the allylic hydrogen atom (Figure 2(b)). This first consists of O-O bond rotation around the O-C axis in order to approach the targeted hydrogen site, which has a barrier of ca. 0.8 kcal/mol within the PMF (see Figure 2(b)). As the hydroxyl O...H bond distance is systematically reduced in the PMF, a free energy barrier of 8.2 \pm 0.2 kcal/mol is observed at a hydroxyl O...H bond distance around 1.5 Å that corresponds to the hydroxyl O-H bond formation and cleavage of the peroxy O-O bond. In the last umbrella sampling step at 1.4 Å, the barrier is overcome, wherein the newly formed hydroxide radical (·OH) departs and cyclohexanone is created. The hydroxide radical (OH) is highly reactive and will abstract hydrogen atoms from nearby molecules, including the methanol produced from the first step of the catalytic cycle (vide infra) or other available solvent molecules (Scheme 2). Both processes occur very rapidly and without a barrier in equilibrium trajectories after the formation of the hydroxide radical (·OH).

3.2 Catalyst recovery

At this stage in the catalytic cycle, cyclohexenone has been obtained and three side products have been created (H2O, CH3OH, and ·OH). From structure INT-1, the catalyst can be recovered within either a "closed" cycle, in which side product are involved in the recovery, or within an "open" cycle, in which an extra methyl hydroperoxide participates in the recovery process.

3.2.1 The closed cycle

The closed cycle utilizes the side products formed from the Hatom abstraction of cyclohexene (being the CH3O(2)H that is hy-

Scheme 2 Activity of ·OH radical in the solution.

drogen bonded to INT-1) and O₂ addition to cyclohexene radical (being ·OH) within catalyst recovery. If the ·OH is formed in close proximity to the INT-1 then there is a high statistical liklihood of its subsequent reaction with CH₃O(2)H, to yield a hydroxymethyl radical (CH₃O(2)·) that may further spontaneously abstract the final hydrogen atom from N(1) in INT-1 to form a second intermediate of the catalytic cycle INT-2 in Figure 1 and Scheme 2 Importantly, the O(2)-H(1) hydrogen bond facilitates (or preorganizes) O(2) being able to abstract H(2) from N(1) to yield the intermediate INT-2. In the instance where the hydroxide radical (·OH) abstracts a hydrogen atom from acetonitrile, the resulting radical H2CCN· is formed, which has the ability to re-enter the hydrogen abstraction cycle. In that event, the open cycle set of pathways (vide infra) may be more likely.

The evolution of 1 to intermediates INT-1 and then INT-2 involves significant changes to the electronic structure. Prior experimental study of related complexes using UV-vis spectroscopy, magnetic susceptibility, and X-ray crystallography, have indicated the switch of the Cu oxidation state (from Cu(II) to Cu(III)) and a dynamic equilibrium between spin states in a square-planar organometallic complex during the catalytic cycle. 27 To examine the change in electronic structure during the formation of the cyclohexenone, Natural Population Analysis (NPA)^[53] was performed and the atomic spin density was analyzed. Both single point and geometry-optimized clusters consisting of the catalyst and two acetonitrile molecules that are closest to the reactive site were examined. The single point calculations employed the PBE/6-311+G(2df,p) functional/basis-set combination, while the geometry optimization was performed with the smaller 6-31G(d) basis, 54,55. As observed in Table 2, the charge of Cu during

Table 2 NPA charges (q) and spin density (ρ) of Cu and its coordinated atoms in catalyst 1 and intermediates INT-1, INT-2, INT-4, and INT-5 obtained from single point PBE/6-311+G(2df,p) calculations sampled from the DFT-MD trajectory.

	1		INT-1		INT-2	
Site	q	ρ	q	ρ	q	ρ
Cu	0.88	0.43	0.92	0.00	0.91	0.00
N(1)	-0.85	0.09	-0.68	0.00	-0.50	0.52
O(n)	-0.52	0.20	-0.91	0.00	-0.78	0.07
N(2)	-0.53	0.07	-0.49	0.00	-0.49	0.01
O(3)	-0.68	0.11	-0.62	0.00	-0.55	0.01
		INT-4		INT-5		
	Site	q	ρ	q	ρ	
	Cu	0.88	0.44	0.90	0.00	
	N(1)	-0.79	0.17	-0.71	0.00	
	O(n)	-0.92	0.02	-0.34	0.00	
	N(2)	-0.46	0.11	-0.50	0.00	
	O(3)	-0.68	0.13	-0.58	0.00	
n = 4 in INT-5, $n = 1$ otherwise.						

the catalytic cycle is relatively unchanged (q_{Cu} ca. 0.9); however, the unpaired electron density is changed from ca. 0.43 in 1 to essentially zero in INT-1 and INT-2. Concomitantly, there is charge migration from N(1) and O(3) (which become less negatively charged) to O(1) (which becomes more negatively charged), while there is growth of unpaired electron density on N(1) during the formation of INT-2. In terms of bond distances given by PBE/6-31G(d) structural optimizations, the Cu-N(1) and Cu-O(1) bonds in 1 are 2.02 Å and 1.85 Å, respectively (Table $\frac{3}{2}$). In intermediate INT-1, the Cu-N(1) distance drops significantly to 1.84 Å (nearly 10 %). The Cu-O(1) bond is somewhat shortened to 1.80 Å. In intermediate INT-2, the Cu-N(1) and Cu-O(1) bonds are 1.84 Å and 1.79 Å, which are nearly the same as in INT-1. The drop in bond distance herein is in good agreement with the experimental and theoretical observations in the previous report of Storr et al. 27, which clearly pointed out the slight decrease of ionic radius of square-planar Cu upon the oxidation from II to III. In that report, the square-planar Cu site was surrounded by two nearly-equivalent O and two nearly-equivalent N ligands. In the Cu(II) state, the experimental (and calculated) Cu-O and Cu-N bonds are 1.89 (1.90) Å and 1.91 (1.93) Å, respectively; while in the Cu(III) state, the experimental (and calculated) Cu-O and Cu-N bonds are 1.84 (1.84) Å and 1.88 (1.87) Å. 27 Interestingly enough, it is observed in this case study that the Cu-N(1) bond length decreases by a greater extent when undergoing transformation from 1 to INT-1. Overall, we observe that the spin state of 1 is doublet, which reveals the Cu(II) oxidation state. The amino group -N(1)H₂ in 1 is converted to the amido group -N(1)H in INT-1, thus, the Cu-N(1) linkage becomes an ionic bond with shortened bond length (1.84 Å). As a result, the overall spin state of INT-1 is singlet, and the Cu site becomes Cu(III). The oxidation state (III) is retained in INT-2, but spin state of the structure is doublet with one unpaired electron residing at the N(1) site.

Within the equilibrated system of INT-2, $CH_2O(2)H$ forms a stable hydrogen bond with N(1) through the N(1)-H(2) and O(2)-H(1) hydrogen bonds, as shown in the RDF plot in Figure S15.

Table 3 The Cu-ligand bond distances (Å) in catalyst 1 and intermediates INT-1, INT-2, INT-4, and INT-5 obtained from PBE/6-31G(d) optimizations.

Bond	1	INT-1	INT-2	INT-4	INT-5
Cu-N(1)	2.02	1.84	1.84	1.86	1.85
Cu-O(n)	1.85	1.80	1.79	2.10	1.85
Cu-N(2)	1.93	1.89	1.88	1.92	1.91
Cu-O(3)	1.90	1.86	1.88	1.86	1.83
n=4 in INT-5 $n=1$ otherwise					

Based upon the spontaneous H-atom abstraction by the methoxy radical from -N(1)H(2) that created **INT-2**, it is considered unlikely that the reverse reaction will contribute to catalyst recovery. As such, to consider how N(1) may recover its H-atoms and the O(1)-O(2) peroxo bond may reform, we first examine the H-atom abstraction from O(1) by the N(1) site.

The intermediate **INT-2** shown is first equilibrated in acetonitrile prior to executing the umbrella sampling along the N(1)...H(1) distance. The process of H-atom transfer starts to occur at 1.7 Å and the N(1)-H(1) distance is at a minimum at 1.16 Å. A free energy barrier of 11.0 ± 0.2 kcal/mol is observed for this process, which creates an O(1) radical (Figure $\Im(a)$). After the last umbrella sampling step, we allow the system to equilibrate, and H(1) maintains its covalent bond with N(1), establishing the intermediate **INT-3**. This intermediate structure forms a long-lived hydrogen bond with methanol (CH₃O(2)H(2)) via the long-range O(2)-H(1) linkage, as illustrated by the RDF data in Figure $\Im(a)$

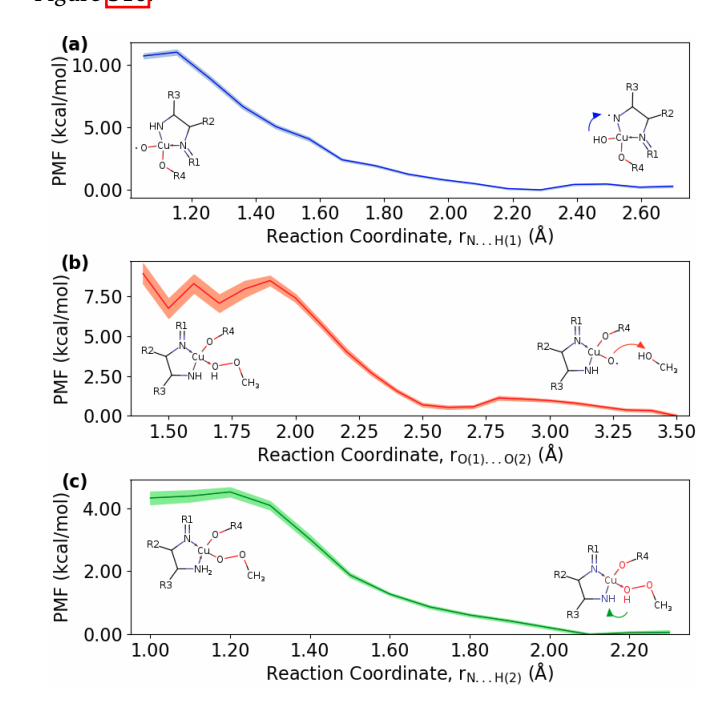


Fig. 3 (a) PMF of the N(1)-H(1) bond formation leading to the establishment of O(1) radical site, to form intermediate INT-3, (b) PMF of the O(1)-O(2) bond formation to re-establish the peroxo bond, (c) PMF of the N(1)-H(2) bond formation to recover the initial catalyst.

The above simulation of N(1)-H(1) recombination allows us to formulate a new perspective about driving forces that may allow

the O(1) and O(2) sites in INT-2 to reform their peroxo bond via the ability of N(1) to abstract an H-atom from O(1), creating a reactive O-site. The next step to recover the initial catalyst is thus explored by sampling the O(1)...O(2) distance coordinate from the equilibrated INT-3, which sets the O(1)-O(2) distance in the system to be around 3.5 Å. During the system equilibration, the RDF for the O(2)-H(1) pair (Figure S16) indicates a hydrogen bond between O(2) and H(1) at around 2 Å. As O(1) approaches closer to O(2) at the local minimum when the O(1)-O(2) distance is 2.7 Å, H(2) quickly migrates toward O(1) and makes a strong covalent bond. After 19 umbrella sampling steps (step size = 0.1Å), the system seems to be trapped in another local minimum where the O-O peroxide distance is around 1.7 Å, as shown in Figure 3(b). Interestingly, when the system is equilibrated for 0.5 ps at the current O(1)-O(2) distance of 1.7 Å, it would favor to release ·CH₃O(2) radical, which can re-enter another catalytic cycle, while the -O(1)-H(2) residue remains bonding with Cu. Later, the actual minimum for the O(1)-O(2) peroxide bond formation is located around 1.5 Å. The free energy barrier of this process is determined as 8.5 ± 0.6 kcal/mol, which is found around the O(1)-O(2) distance of 1.9 Å. Continuing to sample toward the O(1)-O(2) equilibrium distance around 1.4-1.5 Å, we find the that the methyl hydroperoxide (CH₃OOH) that is formed maintains the O(1)-Cu bond.

The last umbrella sampling in this closed cycle is carried out with the recovery of the catalyst, in which we investigate the return of H(2) to N(1). After the O(1)-O(2) peroxide bond is establish, the whole system is equilibrated for 1 ps at 350 K. The equilibrated N(1)-H(2) distance after this process is just 2.3 Å. During the umbrella sampling (Figure 3(c)), the free barrier is 4.5 \pm 0.1 kcal/mol at the N(1)-H(2) of ca. 1.3 Å. After overcoming the harmonic sampling step around 1.2 Å, the original structure of catalyst is finally recovered.

The overall reaction mechanism observed by umbrella sampling MD in this closed cycle is presented in Scheme 3. It should be noted that we only present the primary reaction channels with the most favorable free energies barriers in the scheme. Overall, a water molecule is obtained as a side product besides the targeted product, cyclohexenone. Although methanol is formed as an intermediate product, it is consumed when the original catalyst is restored. The energetic span for this closed cycle is presented in Figure S19. In this energetic span, we had to approximate the free energy of INT-1 being converted to INT-2. This free energy cannot be determined using the statistical umbrella sampling method due to extremely high activity when OH participates in the catalyst recovery cycle (see Scheme 2), we thus employ an approximation based on total electronic energies. The difference in total electronic energy of INT-1 before the conversion step and INT-2 after conversion is the difference in free energy. The energy span δE (Equation 4) for this closed cycle consumes 26.2 kcal/mol in comparison to the experimental estimate from the TOF of 22.7 kcal/mol.

3.2.2 The open cycle

In comparison to the closed cycle, the open cycle avoids the formation of an O-O bond within catalyst recovery by ignoring the

Scheme 3 The allylic oxidation scheme in the closed catalyst-recovery cycle.

participation of the side products in the formation of INT-1 and instead allowing entry of the alkyl hydroperoxide which is present under reaction conditions. Starting from INT-1, CH₃OOH reacts with the -O(1)H bound to Cu, to produce H₂O (which is released into solution) and CH₃OO· (which coordinates to the Cu-site). This is followed by rehydrogenation of the -N(1)H by methyl hydroperoxide to recover the catalyst **1**.

The system containing INT-1 and CH₃OOH is equilibrated for 1 ps. For convenience, we denote the active H-atom of the methyl hydroperoxide as H(3) and the oxygen it is bound to as O(4), while the O-atom of the Cu-bound -OH is O(1). Testing of the O(1)-H(3) reaction coordinate revealed no minima in the PMF (Figure $\frac{1}{4}$ (a)) and further no-dissociation of the O(4)-H(3) bond althought it elongates to 1.4 Å. These data indicate a more complex and higher dimensional reaction coordinate (for example a 2-dimensional coordinate consisting of both the O(1)-H(3) and methyl hydroperoxide O(4)-H(3)) for the formation of H₂O and CH₃OO·. Complete sampling of the 2D PMF is computationally impractical and as an alternative a slice of this 2D surface was instead examined with the O(1)-H(3) distance fixed at 1.05 Åand a PMF along the O(4)-H(3) distance. The 1.05-Å O(1)-H(3) constraint is chosen because it is close to the transition state of O(1)-H(3) bond formation, where it requires 3.7 \pm 0.2 kcal/mol.

The sampling for the O(4)-H(3) bond dissociation is begins at 1.4 Å, which is the equilibrium distance at O(1)-H(3) of 1.05 Å. After only 5 umbrella sampling steps, at the CH₃OO(4)-H(3) distance of 1.7 Å, the system reaches a transition state, and the expected products (H2O and CH3OO) are formed in the next umbrella sampling bin. The free energy for the O(4)-H(3) bond rupture is 1.3 \pm 0.1 kcal/mol (Figure $\frac{4}{5}$ (b). The structure obtained at this point is labelled **INT-4** (Figure 1). Static PBE-D3 optimization and NPA analysis reveals that although INT-1 is a singlet Cu(III), the spin state of **INT-4** is doublet Cu(II) (Table 2). However INT-4 is unstable, as indicated by the departure of the bound H2O during 0.5 ps of DFT-MD equilibration. After the departure

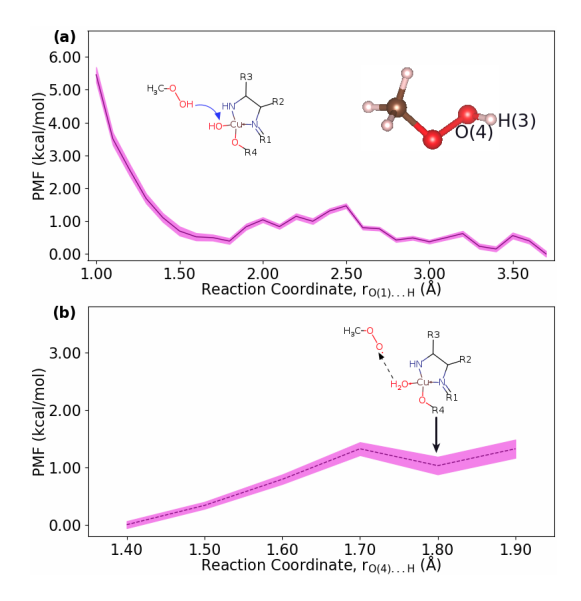


Fig. 4 Energy contributions for the formation of INT-4. (a) PMF of the O(1)-H(3) reaction coordinate for methyl hydroperoxide attack on the -O(1)H bound to Cu, (b) PMF of the O(4)...H(3) dissociation at a fixed O(1)-H(3) distance of 1.05 Å(using the zero of energy in (a) as the reference).

of the H2O ligand, umbrella sampling mapped the potential of mean force for $CH_3OO(4)$ coordination to Cu site to form **INT-5** (Figure 517), however there is no activation energy and only a exergonic process that releases 4.6 kcal/mol when the Cu-O(4) equilibrium distance is attained around 1.9 Å. Upon binding to the Cu site, the $CH_3OO(4)$ induces Cu oxidation in **INT-5** to form Cu(III) (Table 2).

The last reaction step of the open cycle is the H-atom transfer from another HOOCH3 molecule to the N(1) site. This step converts the amido ligand -N(1)RH to amino -NRH2, and yields back the Cu(II) oxidation state. After equilibrating the system containing INT-5 and HOOCH3, we start our umbrella sampling investigation from the N(1)...H(4) distance of 2.2 Å. At 1.9 Å, a local minimum is identified due to the hydrogen bond of the N(1)-H(4) pair (Figure \$18(a)). Performing umbrella sampling toward the formation of N(1)-H(4) bond, we observe no local minimum as an indication of H(4)-O(5)OCH₃ bond rupture. At the N(1)-H(4) distance of 1.05 Å, the free energy is 4.5 \pm 0.1 kcal/mol, which is close to the transition state of bond formation. We again perform additional umbrella sampling for the breaking of H(4)-O(5)OCH₃ bond while the N(1)-H(4) distance is constrained at 1.05 Å. The H-OOCH₃ bond rupture can be observed at 2.2 Å, as shown in Figure \$18(b). The additional free energy to break the H(4)-O(5)OCH₃ bond is only 1.9 \pm 0.1 kcal/mol. Overall, \approx 6.4 kcal/mol is needed for the transfer of H(4) from HOOCH₃ to the N(1) site to restore the original catalyst structure. The reaction scheme involving the open catalyst recovery cycle is shown in Scheme 4. The energy span of the open cycle is presented in Figure \$20, in which we show the relative free energy from the initial H-atom abstraction step to the point where the original catalyst can be retrieved by a two-step reaction with CH₃OOH molecules. According to the open catalyst recovery scheme, the TDTS is the

 $\begin{tabular}{ll} Scheme & 4 & The allylic oxidation scheme in the open catalyst-recovery cycle. \end{tabular}$

final transition state before reverting back to the original catalyst structure **1**. The energy span for the reaction cycle using Equation is 16.5 kcal/mol, nearly 10 kcal/mol lower than that observed for the closed cycle.

Comparison of the closed and open cycle pathways reveals several distinguishing characteristics for consideration. The cycles branch after the formation of INT-1 and thus both encompass the Cu(II) to Cu(III) oxidation, and both further contain the Cu(III) to Cu(II) recovery. Importantly, the closed cycle contains both O-O breaking and formation events, the latter appearing antithetical to the premise of using an alkyl hydroperoxide oxidant. While the energy span of the closed cycle is closer to that estimated from the experimental TOF (26.2 kca/mol vs. 22.7 kcal/mol experimentally), it is nearly 10 kcal/mol higher in energy than the open cycle. The closed cycle further contains more efficiency in accounting for side products and produces less radical side products. The open cycle leverages the alkyl hydroperoxide during catalyst recovery and does not lead to any O-O bond forming steps. It further does not mandate a second dehydrogenation of the bound amide. Yet it leads to production of both hydroxyl and methylperoxide radical side products.

4 Conclusions

Two complete catalytic mechanisms of allylic oxidation of cyclohexenone by a Cu(II) complex have been identified by DFT-MD, wherein the the ensemble of configurations of acetonitrile solvation and dynamically evolving degrees of freedom of the solute and solvent identify new reaction branches and side processes. The first cycle incorporates side products within catalyst recovery and is labelled the "closed" cycle, while the second cycle incorporates the alkyl hydroperoxide oxidant and is labelled the "open" cycle. The closed cycle has a predicted energy span of

26.2 kcal/mol while the open cycle has a predicted value of 16.5 kcal/mol at 350 K. These data compare to an estimated experimental value of 22.7 kcal/mol at 350 K. The reactions branch after the allylic H-atom abstraction which creates a Cu(III) intermediate based upon dehydrogenation of the bound -NH2 of the ligand, where the Cu oxidation consistent with prior experimental studies. The reversible dehydrogenation/rehydrogenation of the amido group is the key to the overall mechanism and catalyst recovery. Multiple instances are observed throughout both catalytic cycles that rely upon the ensemble sampling of configurations of the reactants and stabilization by explicit solvation, pointing to the importance of DFT-MD as a tool to provide new insight about catalytic processes in multicomponent solutions.

Conflicts of interest

There are no conflicts to declare.

Acknowledgements

We are thankful to the computational resource from the Center for Institutional Research Computing, Washington State University (Pullman, WA) and partially from the Center for Computational Materials Science, Tohoku University (Tohoku, Japan). This work was funded by a grant from the National Science Foundation, award number OAC-1934725.

Notes and references

- 1 S. Danishefsky and M. Kahn, Tetrahedron Letters, 1981, 22, 489 - 492.
- 2 R. Ballini and G. Bosica, Tetrahedron, 1995, **51**, 4213 4222.
- 3 J. Salva and D. J. Faulkner, The Journal of Organic Chemistry, 1990, **55**, 1941–1943.
- 4 R. Ballini and G. Bosica, Tetrahedron Letters, 1996, 37, 8027 - 8030.
- 5 Y. Liu, X. Liu, M. Wang, P. He, L. Lin and X. Feng, The Journal of Organic Chemistry, 2012, 77, 4136-4142.
- 6 A. Nakamura and M. Nakada, Synthesis, 2013, 45, 1421-1451.
- 7 V. Weidmann and W. Maison, Synthesis, 2013, 45, 2201-2221.
- 8 R. A. Miller, W. Li and G. R. Humphrey, Tetrahedron Letters, 1996, 37, 3429 – 3432.
- 9 J. Salvador, M. Sáe Melo and A. Campos Neves, Tetrahedron Letters, 1997, 38, 119 - 122.
- 10 J.-Q. Yu, H.-C. Wu and E. J. Corey, Organic Letters, 2005, 7, 1415-1417.
- 11 M. A. Fousteris, A. I. Koutsourea, S. S. Nikolaropoulos, A. Riahi and J. Muzart, Journal of Molecular Catalysis A: Chemical, 2006, **250**, 70 - 74.
- 12 S. M. Silvestre and J. A. Salvador, Tetrahedron, 2007, 63, 2439
- 13 E. C. McLaughlin, H. Choi, K. Wang, G. Chiou and M. P. Doyle, The Journal of Organic Chemistry, 2009, 74, 730-738.
- 14 B. Yao, D.-X. Wang, Z.-T. Huang and M.-X. Wang, Chem. Commun., 2009, 2899-2901.

- 15 H. Wang, Y. Wang, D. Liang, L. Liu, J. Zhang and Q. Zhu, Angewandte Chemie International Edition, 2011, 50, 5678-5681.
- 16 P. Pirovano, A. M. Magherusan, C. McGlynn, A. Ure, A. Lynes and A. R. McDonald, Angewandte Chemie International Edition, 2014, 53, 5946-5950.
- 17 A. H. Abazid, N. Clamor and B. J. Nachtsheim, ACS Catalysis, 2020, 10, 8042-8048.
- 18 S. Muthuramalingam, K. Anandababu, M. Velusamy and R. Mayilmurugan, Inorganic Chemistry, 2020, 59, 5918-5928.
- 19 X. Wu and A. E. V. Gorden, European Journal of Organic Chemistry, 2009, 2009, 503-509.
- 20 Y. Li, T. B. Lee, T. Wang, A. V. Gamble and A. E. V. Gorden, The Journal of Organic Chemistry, 2012, 77, 4628-4633.
- 21 R. Trammell, K. Rajabimoghadam and I. Garcia-Bosch, Chemical Reviews, 2019, 119, 2954-3031.
- 22 Y. Li, T. Lee, K. Weerasiri, T. Wang, E. E. Buss, M. L. McKee and A. E. V. Gorden, Dalton Trans., 2014, 43, 13578-13583.
- 23 S. Kozuch and S. Shaik, Accounts of Chemical Research, 2011, 44, 101-110.
- 24 J. S. Tse, Annual Review of Physical Chemistry, 2002, 53, 249-
- 25 R. Car, Quantitative Structure-Activity Relationships, 2002, 21, 97-104.
- 26 R. Iftimie, P. Minary and M. E. Tuckerman, Proceedings of the National Academy of Sciences, 2005, 102, 6654-6659.
- 27 T. Storr, P. Verma, R. C. Pratt, E. C. Wasinger, Y. Shimazaki and T. D. P. Stack, Journal of the American Chemical Society, 2008, **130**, 15448–15459.
- 28 L. Martínez, R. Andrade, E. G. Birgin and J. M. Martínez, Journal of Computational Chemistry, 2009, 30, 2157-2164.
- 29 G. Bussi, T. Zykova-Timan and M. Parrinello, The Journal of Chemical Physics, 2009, 130, 074101.
- 30 P. Giannozzi, O. Andreussi, T. Brumme, O. Bunau, M. B. Nardelli, M. Calandra, R. Car, C. Cavazzoni, D. Ceresoli, M. Cococcioni, N. Colonna, I. Carnimeo, A. D. Corso, S. de Gironcoli, P. Delugas, R. A. D. Jr, A. Ferretti, A. Floris, G. Fratesi, G. Fugallo, R. Gebauer, U. Gerstmann, F. Giustino, T. Gorni, J. Jia, M. Kawamura, H.-Y. Ko, A. Kokalj, E. Küçükbenli, M. Lazzeri, M. Marsili, N. Marzari, F. Mauri, N. L. Nguyen, H.-V. Nguyen, A. O. de-la Roza, L. Paulatto, S. Poncé, D. Rocca, R. Sabatini, B. Santra, M. Schlipf, A. P. Seitsonen, A. Smogunov, I. Timrov, T. Thonhauser, P. Umari, N. Vast, X. Wu and S. Baroni, Journal of Physics: Condensed Matter, 2017, 29, 465901.
- 31 J. P. Perdew, K. Burke and M. Ernzerhof, Phys. Rev. Lett., 1996, 77, 3865-3868.
- 32 J. P. Perdew, K. Burke and M. Ernzerhof, Phys. Rev. Lett., 1997, 78, 1396-1396.
- 33 Y. Zhang and W. Yang, Phys. Rev. Lett., 1998, 80, 890-890.
- 34 S. Grimme, J. Antony, S. Ehrlich and H. Krieg, The Journal of Chemical Physics, 2010, 132, 154104.
- 35 D. Vanderbilt, Phys. Rev. B, 1990, 41, 7892-7895.
- 36 A. M. Rappe, K. M. Rabe, E. Kaxiras and J. D. Joannopoulos, Phys. Rev. B, 1990, 41, 1227-1230.

- 37 A. Dal Corso, Computational Materials Science, 2014, 95, 337 - 350.
- 38 L. Verlet, Phys. Rev., 1967, 159, 98-103.
- 39 G. Torrie and J. Valleau, Journal of Computational Physics, 1977, **23**, 187 – 199.
- 40 J. Kästner, Computational Molecular Science, 2011, 1, 932-942.
- 41 W. You, Z. Tang and C.-e. A. Chang, Journal of Chemical Theory and Computation, 2019, 15, 2433-2443.
- 42 E. Braun, S. M. Moosavi and B. Smit, Journal of Chemical Theory and Computation, 2018, 14, 5262-5272.
- 43 B. Roux, Computer Physics Communications, 1995, 91, 275 -
- 44 S. Kumar, J. M. Rosenberg, D. Bouzida, R. H. Swendsen and P. A. Kollman, Journal of Computational Chemistry, 1992, 13, 1011-1021.
- 45 A. Grossfield, WHAM: an implementation of the weighted histogram analysis method, version 2.0.9, http://membrane. urmc.rochester.edu/content/wham/.
- 46 R. C. Binning Jr. and L. A. Curtiss, Journal of Computational Chemistry, 1990, 11, 1206–1216.

- 47 L. A. Curtiss, M. P. McGrath, J. Blaudeau, N. E. Davis, R. C. Binning and L. Radom, The Journal of Chemical Physics, 1995, **103**, 6104–6113.
- 48 A. V. Marenich, C. J. Cramer and D. G. Truhlar, The Journal of Physical Chemistry B, 2009, 113, 6378-6396.
- 49 J. Tomasi, B. Mennucci and R. Cammi, Chemical Reviews, 2005, 105, 2999-3094.
- 50 Q. Liao, Computational Approaches for Understanding Dynamical Systems: Protein Folding and Assembly, Academic Press, 2020, vol. 170, pp. 177 - 213.
- 51 M. Besora, P. Vidossich, A. Lledós, G. Ujaque and F. Maseras, The Journal of Physical Chemistry A, 2018, 122, 1392–1399.
- 52 L. Watson and O. Eisenstein, Journal of Chemical Education, 2002, 79, 1269.
- 53 F. Martin and H. Zipse, Journal of Computational Chemistry, 2005, 26, 97-105.
- 54 G. A. Petersson, A. Bennett, T. G. Tensfeldt, M. A. Al-Laham, W. A. Shirley and J. Mantzaris, The Journal of Chemical Physics, 1988, 89, 2193-2218.
- 55 G. A. Petersson and M. A. Al-Laham, The Journal of Chemical Physics, 1991, 94, 6081-6090.